ES Materials & Manufacturing

RESEARCH PAPER

View Article Online

Facile Fabrication Hierarchical Pore Structure $Li_{1.2}Mn_{0.54}Ni_{0.13}Co_{0.13-x}Sr_xO_2$ Nanofiber for High-Performance Cathode Materials in Li-ion Battery

Yu Zhang, Xingyu Li, Tianjiao Zhu, Shulan Ma, Huifeng Li and Genban Sun*

The long-cycle life cathode material plays a key role in terms of energy and power density for lithium ion battery. In this work, a series of Sr-doped hierarchical porous nanofiber structure $Li_{1.2}Mn_{0.54}Ni_{0.13}Co_{0.13-x}Sr_xO_2$ are synthesized via electrospinning combined with high temperature solid phase technology. As a result, Sr-doping can enhance the cyclic performance, suppress the voltage decay and stabilize the structure. With the incorporation of Sr, not only the crystal structure and morphology of $Li_{1.2}Mn_{0.54}Ni_{0.13}Co_{0.13-x}Sr_xO_2$ are slightly changed, but also both the specific capacity and discharge voltage of the Li rich cathode are stabilized upon cycling. When x = 0.03, $Li_{1.2}Mn_{0.54}Ni_{0.13}Co_{0.1}Sr_{0.03}O_2$ delivers an initial discharge capacity of 213 mAh g^{-1} and a capacity retention of 94.16 % at the 100th cycle. The influence of the percentage of dopeed Sr on the performance of the battery is analyzed. Rational Sr dopeing technology is an effective way to improve the electrochemical performance of Li rich manganese based material.

Keywords: Nanofibers; Sr-doping, Lithium-rich; Lithium-Ion Battery

Received 10 October 2018, **Accepted** 6 December 2018

DOI: 10.30919/esmm5f201

Introduction

Because of the energy shortage and the emergence of portable electronic equipment and electric vehicles, rechargeable lithium-ion batteries (LIBs) have attracted wide attention and played a leading role in energy storage.[1-2] Compared to other energy storage devices, lithium-ion batteries possess numerous advantages, such as high energy density, long cycle life and environmental benignity. Cathode material plays a key role in terms of energy and power density for a LIBs. Lithium-rich manganese-based layered oxide, usually denoted as $xLi_2MnO_3\cdot(1-x)LiMO_2$ (M = Mn, Co, Ni, etc.), is considered to be the most promising cathode material because it can deliver a discharge capacity up to 250 mAh g^{-1}, which is significantly greater than the current commercialized cathode materials. According to reports, these materials integrate two different local structures into a solid solution, one with a rhombohedral $LiMO_2$ (space group R-3m) and the other with a monoclinic Li_2MnO_3 (space group C2/m). When charged to potentials higher than 4.5 V, these materials are able to achieve their high specific capacity, which is associated with the irreversible activation of Li_2MnO_3[3-4]. However, these Li-rich cathodes have fatal drawbacks, such as large irreversible capacity loss at the initial cycle, voltage decays and layered-to-spinel phase transformation during cycling, which directly impede the commercialization of Li-rich cathodes in high-energy-density lithium-ion batteries.

To improve the electrochemical properties of these Li-rich cathode materials, considerable endeavors have been devoted. One possible strategy is surface modification. For instance, coating the lithiated metal fluoride[5-6] or oxide[7-8] with nano-sized is a versatile method, it can avoid direct contact between active materials and electrolyte, and effectively inhibit interfacial side reactions. Zhao *et al.*[6] synthesized the LiF/FeF_3 nanoparticles coated Li-rich $Li[Li_{0.2}Ni_{0.2}Mn_{0.6}]O_2$ cathode via a facile aqueous solution process, and this novel composite cathode showed high electrochemical performance. Kobayashi *et al.*[7] reported that the discharge capacity can achieve higher than 310 mAh g^{-1} through surface modification of $Li[Li_{0.2}Ni_{0.18}Co_{0.03}Mn_{0.58}]O_2$ with Al_2O_3. Besides, decorating the surface of Li-rich cathode materials with spinel membrane is another tactic to improve battery performance. Wu *et al.*[9] reported an ultrathin spinel membrane-encapsulated layered lithium-rich cathode, where the voltage decay and thermal instability were found to be alleviated. However, the surface modification cannot obstruct the voltage degradation upon cycling led by the layered-to-spinel phase transformation.

There are indications that doping or substituting additional ions such as Al^{3+}[10-11], Mg^{2+}[12-13], K^+[14], Mo^{6+}[15-17], Y^{3+}[18-19] and La^{3+}[20] into lithium-rich Mn-based materials could availably stabilize the host structure. Nayak *et al.*[11] substituted Mn in Li cathode materials $Li_{1.2}Mn_{0.56}Ni_{0.16}Co_{0.08}O_2$ by Al and reported that Al substitution has a bulk stabilizing effect on the layered $LiMO_2$ phase. Yu *et al.*[20] synthesized La-doped lithium-rich layered oxide materials $Li_{1.2}Mn_{0.54-x}Ni_{0.13}Co_{0.13}La_xO_2$ (x= 0.01, 0.02, 0.03). This material exhibits 93.2 % capacity retention after 100 cycles at 1 C. Moreover, La doping can stabilize the layered framework upon long term cycling and suppress voltage fading. Sun *et al.*[18] reported a Y-doped layered cathode material $Li[Li_{0.2}Ni_{0.2-x/2}Mn_{0.6-x/2}Y_x]O_2$ with better electrochemical performance. Y-doping not only decreases electrochemical polarization and charge-transfer resistance, but also enhances the ability of Li^+ diffusion.

Strontium (Sr) has been used as substitution element in many cathode materials, such as $LiCoO_2$[21], $LiNi_{0.8}Co_{0.2}O_2$[22] and $LiMn_2O_4$[23], for Sr^{2+} possess large radius and keep inactive during the electrochemical

Beijing Key laboratory of Energy Conversion and Storage Materials, college of chemistry, Beijing Normal University, Beijing 100875, China
***E-mail:** lihuifeng@bnu.edu.cn; gbsun@bnu.edu.cn*

process. To the best of our knowledge, Li-rich materials are composed by Li_2MnO_3 component and $LiNi_{1/3}Co_{1/3}Mn_{1/3}O_2$ component and the ternary component plays an important role in the electrochemical process. Thus, Sr substitution for partial redox active Co in the $LiNi_{1/3}Co_{1/3}Mn_{1/3}O_2$ component of Li-rich material may reduce the initial discharge capacity, but it expands and stabilizes the pathway for intercalation and deintercalation of Li^+, which could enhance the rate capacity and suppress the voltage and capacity fading during cycling.

In this work, a series of the Li-rich Sr-doped nanofiber structure $Li_{1.2}Mn_{0.54}Ni_{0.13}Co_{0.13-x}Sr_xO_2$ were synthesized via electrospinning combined with high temperature solid phase reaction technology. The effects of Sr substitution for partial Co on the structure, morphology, electrochemical properties and electron conductivity of the $Li_{1.2}Mn_{0.54}Ni_{0.13}Co_{0.13}O_2$ are systematically studied.

Experimental

Sample synthesis

The Sr-doped layered $Li_{1.2}Mn_{0.54}Ni_{0.13}Co_{0.13-x}Sr_xO_2$ (x=0, 0.01, 0.03, 0.05) nanofibers cathode materials were synthesized by the combination of electrospinning and a subsequent heat treatment. The 1.6 g of Polyacrylonitrile (PAN) was dissolved in 15 ml of N, N-dimethylformamide (DMF) solution with stirring for 12 h to obtain a homogeneous solution, here marked as solution A. The designated compositions with stoichiometric amount of $LiCH_3COO·2H_2O$, $Ni(CH_3COO)_2·4H_2O$, $Mn(CH_3COO)_2·4H_2O$, $Co(CH_3COO)_2·4H_2O$ and $Sr(CH_3COO)_2·4H_2O$ were dissolved in 10 ml of DMF solution with stirring for 12 h, here marked as solution B. Then, solution A and solution B were mixed together with continuous stirring for 12 h at ambient temperature until a homogeneous electrospinning solution was obtain. Next, the mixed solution was subjected to electrospinning with a flow rate of 5 mL h^{-1}, and a distance of 15 cm between the tip and collector. Under a voltage of 13 kV, a white as-spun nanofibers film was collected on an aluminum foil. Finally, to obtain crystallized cathode materials with nanofibers, the white as-spun nanofibers film were initially stabilized at 280 °C for 4 h and then calcined at 800 °C for 12 h in air with a heating rate of 2 °C min^{-1}.

Structural characterization

The crystal phase of the materials was characterized by Powder X-ray diffraction (XRD, Shimadzu XRD-7000, Cu Kα radiation, Japan) with a scan rate of 5° Min^{-1} from 10° to 80° (2θ). The morphology and further structural characteristics of these cathode materials were observed by field emission scanning electron microscope (FESEM, Hitachi SU8010, Japan) and high-resolution transmission electron microscope (HRTEM, JEM-2010, JEOL, Japan). Raman spectroscopic studies of materials were carried out using a microscopic confocal Raman spectrometer (LabRAMAramis, Horiba Jobin Yvon) equipped with a 532 nm He-Ne laser, and the scanning range was from 200 to 1000 cm^{-1}. X-ray photoelectron spectroscopy (XPS, ESCALAB 250Xi, America) was performed to determine the surface chemical states of the samples. Inductively coupled plasma-atomic emission spectrum (ICP-AES, Jarrel-ASH, ICP-9000) was employed to analyze the chemical compositions of as-prepared samples.

Electrochemical characterization

The electrochemical properties of $Li_{1.2}Mn_{0.54}Ni_{0.13}Co_{0.13-x}Sr_xO_2$ (x=0, 0.01, 0.03, 0.05) were examined by using coin-type cells CR-2032. The electrodes were prepared by mixing the active materials (80 wt%), conductive acetylene black (10 wt%) and polyvinylidene fluoride (PVDF) (10 wt%) in N-methyl-2-pyrrolidone and stirred for 1 h to obtain slurry. The slurry was evenly coated on aluminum foil and dried at 110 °C for 12 h in vacuum oven. The cells were assembled in an Ar-filled glovebox (M.Braun, Labstar, Germany) with lithium foil as the counter electrode, Celgard 2400 as the separator, and the 1 M $LiPF_6$ in ethyl carbonate (EC) and diethyl carbon (DEC) (volume ratio is 1: 1) as the electrolyte. Galvanostatic charge-discharge tests were implemented at room temperature on the Neware (China) battery test system in the voltage range from 2.0 V to 4.8 V vs Li^+/Li (1 C = 280 mA g^{-1}).

Results and discussion

Materials composition and structure

The atomic compositions of as-obtained material are confirmed by inductive coupled plasma (ICP) technique, and the elemental analysis results are tabulated in Table 1. Accroding to the results, the composition of the as-synthesized materials are found to be very close to the targeted compositions. Especially, the concentration of Sr in each sample is aggrement with the nominal stoichiometry and the Co content decreases with the increase of Sr, as expected.

Fig. 1a demonstrates the X-ray diffration (XRD) patterns of the obtained $Li_{1.2}Mn_{0.54}Ni_{0.13}Co_{0.13-x}Sr_xO_2$ (x= 0, 0.01, 0.03, 0.05) powders. The diffraction peaks of all samples, except 2θ=20~25°, can be indexed as the hexagonal α-$NaFeO_2$ layered structure with an R-3m space group.[24-26] These weak diffraction peaks at 2θ=20~25° are considered to be related to the super lattice cation ordering of $LiMn_6$ in the transition metal layers, confirm the existence of Li_2MnO_3.[4] There is a slight peak shift but no noticeable impurity phase in the XRD patterns, which reveals the Sr doping is valid but it does not change the crystal structure significantly. Meanwhile, two pairs of the (006)/ (012) peaks and the (108)/ (110) peaks are well spilt, suggests the formation of a well-ordered layered structure for all samples with Sr-doping.[27]

The Raman spectra of pristine ($Li_{1.2}Mn_{0.54}Ni_{0.13}Co_{0.13}O_2$) and the modified ($Li_{1.2}Mn_{0.54}Ni_{0.13}Co_{0.10}Sr_{0.03}O_2$) samples are shown in Fig. 1b. Both

Table 1 The theoretical and experimental results of Li:Mn:Ni:Co:Sr molar ratios of the electrode materials according to ICP analysis.

Sample	Theoretical molar ratios of Li:Mn:Ni:Co:Sr	Experimental molar ratios of Li:Mn:Ni:Co:Sr
$Li_{1.2}Mn_{0.54}Ni_{0.13}Co_{0.13}O_2$	1.2:0.54:0.13:0.13:0	1.190:0.552:0.129:0.134:0
$Li_{1.2}Mn_{0.54}Ni_{0.13}Co_{0.12}Sr_{0.01}O_2$	1.2:0.54:0.13:0.12:0.01	1.196:0.591:0.129:0.125:0.011
$Li_{1.2}Mn_{0.54}Ni_{0.13}Co_{0.10}Sr_{0.03}O_2$	1.2:0.54:0.13:0.10:0.03	1.200:0.589:0.130 :0.095:0.033
$Li_{1.2}Mn_{0.54}Ni_{0.13}Co_{0.08}Sr_{0.05}O_2$	1.2:0.54:0.13:0.08:0.05	1.216:0.586:0.129:0.083:0.050

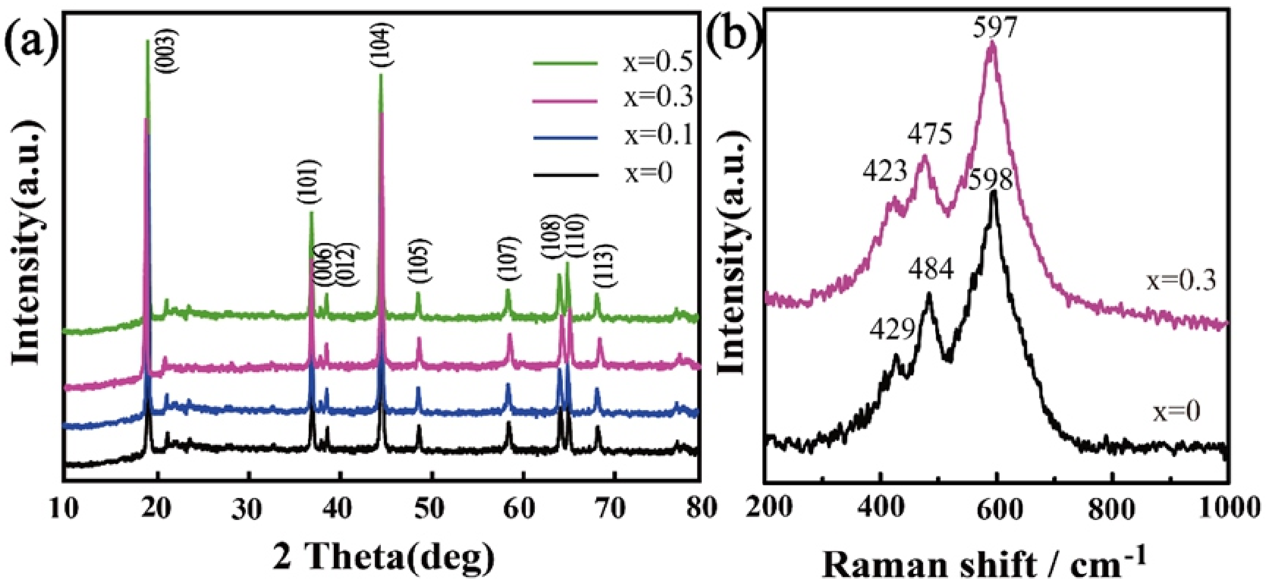

Fig. 1 (a) XRD patterns of $Li_{1.2}Mn_{0.54}Ni_{0.13}Co_{0.13-x}Sr_xO_2$ (x=0, 0.01, 0.03, 0.05); (b) Raman spectra of $Li_{1.2}Mn_{0.54}Ni_{0.13}Co_{0.13-x}Sr_xO_2$ (x=0, 0.03) samples.

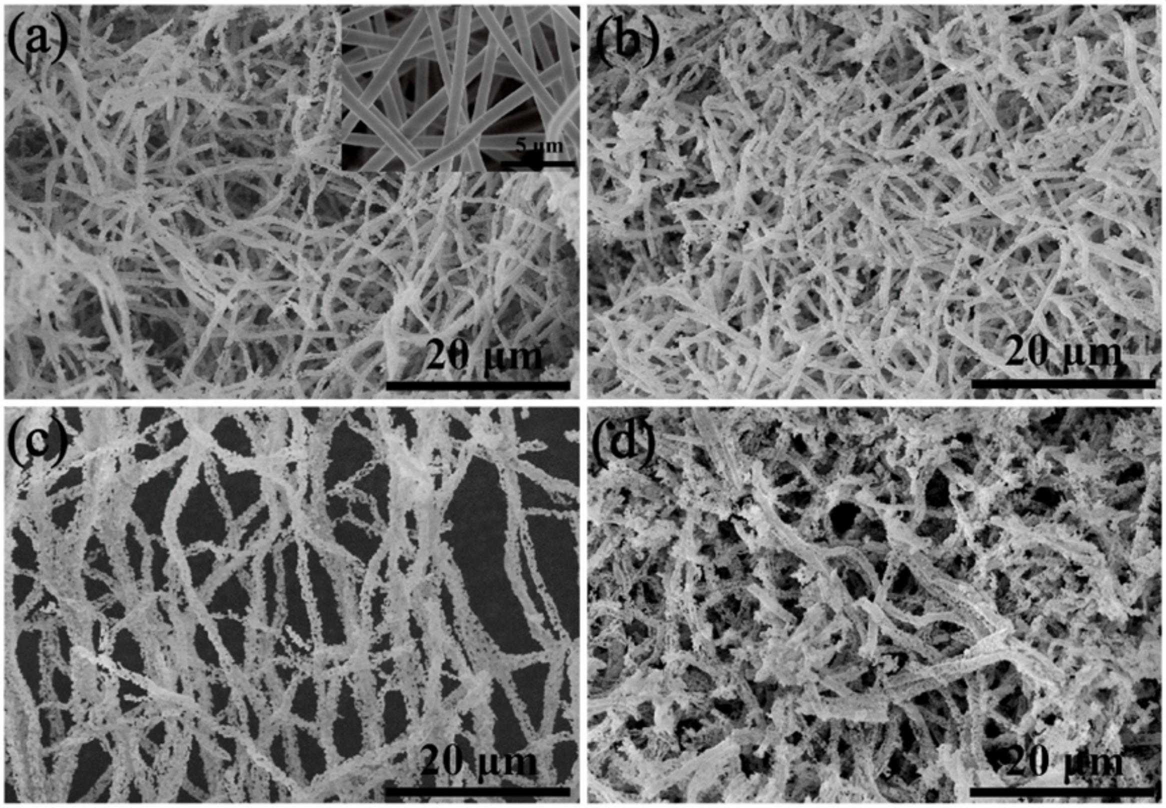

Fig. 2 SEM images of $Li_{1.2}Mn_{0.54}Ni_{0.13}Co_{0.13-x}Sr_xO_2$ samples (a) x=0, (b) x=0.01, (c) x=0.03 and (d) x=0.05. The image of inset in Fig. (a) is precursor nanofibers of $Li_{1.2}Mn_{0.54}Ni_{0.13}Co_{0.13}O_2$.

samples present three characterisitic Raman bands of $Li_{1.2}Mn_{0.54}Ni_{0.13}Co_{0.13}O_2$ at around 429, 484 and 598 cm^{-1} in the range of 100-1000 cm^{-1}. The weak Raman band which appears at 429 cm^{-1} is ascribed to the vibration of monoclinic Li_2MnO_3 phase.[28] The other two Raman bands at around 484 cm^{-1} and 598 cm^{-1} are assigned to the E_g and A_{1g} vibration mode of Raman-active $LiMO_2$ phase, respectively.[29-31] Obviously, in the Raman spectra of un-doped ($Li_{1.2}Mn_{0.54}Ni_{0.13}Co_{0.13}O_2$) and Sr-doping ($Li_{1.2}Mn_{0.54}Ni_{0.13}Co_{0.10}Sr_{0.03}O_2$) sample, the position and intensity of the three bands are barely the same, which indicates that the Sr-doping does not change the structure of the $Li_{1.2}Mn_{0.54}Ni_{0.13}Co_{0.10}Sr_{0.03}O_2$ sample significantly again.

Microscopic morphology

The morphology of pristine and Sr-doped ($Li_{1.2}Mn_{0.54}Ni_{0.13}Co_{0.13-x}Sr_xO_2$

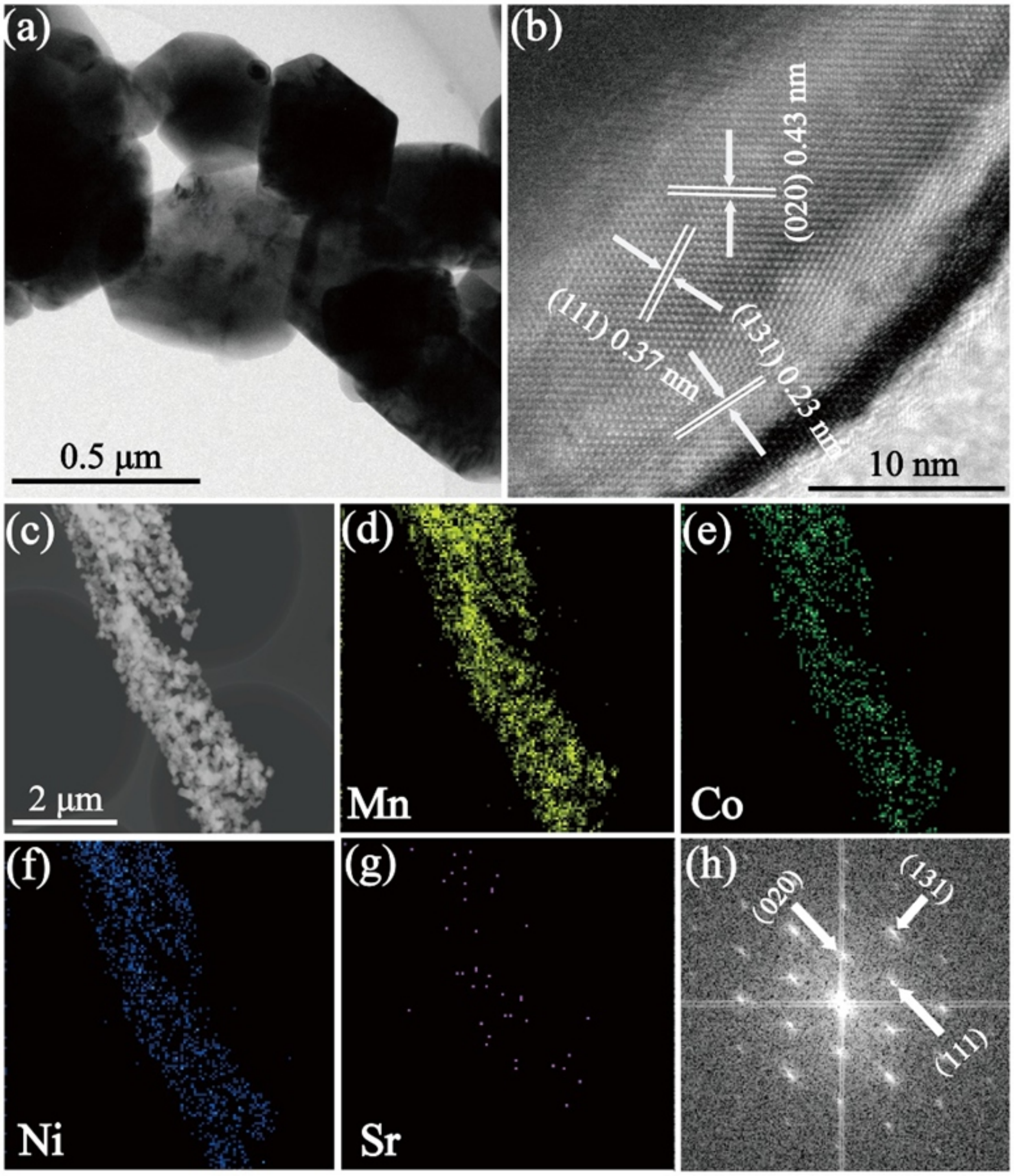

Fig. 3 The image of $Li_{1.2}Mn_{0.54}Ni_{0.13}Co_{0.10}Sr_{0.03}O_2$ (a) TEM, (b) HRTEM. (c-g) EDS elemental mapping with respect to Mn, Co, Ni, Sr, receptivity. (h) Fast Fourier transform patterns of the selected area in image (b).

(x=0, 0.01, 0.03, 0.05)) samples were characterized by scanning electron microscopy (SEM). As being seen from Fig. 2, four different types of cathode materials with complex one dimension (1D) nanofiber structures have been successfully prepared by electrospinning technology. The inset of Fig. 2a displays the as-spun precursor nanofiber with a smooth surface and continuous uniform features with an average diameter of around 800 nm. After calcination at 800 centigrade degree, the diameter of 1D nanofiber structures decreases to around 700 nm and a large amount of pores are generated, which might be caused by the decomposition of metal precursor and removal of polymer components. With the incorporation of Sr ion, the morphology of materials is not distinctly changed and the nanofiber structure remains well. However, it is worth pointing out that the diameter of nanofiber materials with different Sr concentration exhibit slight difference, which is mainly due to the secondary particle average size increasing slightly with the increases of Sr component.

The detailed crystal structure and elements distribution in Sr-doped samples were further investigated by high-resolution transmission electron microscopy (HRTEM) and energy dispersive spectroscopy (EDS) elemental mapping. Fig. 3a shows the TEM images of a randomly selected $Li_{1.2}Mn_{0.54}Ni_{0.13}Co_{0.10}Sr_{0.03}O_2$ particle, which is nanofiber morphology composed of primary particles. According to the elemental mapping displayed in Fig. 3c-f, different elements in $Li_{1.2}Mn_{0.54}Ni_{0.13}Co_{0.10}Sr_{0.03}O_2$ sample with respect to Mn, Co, Ni and Sr are uniformly distributed throughout the nanofibers, and Fig. 4 also exhibits the SEM image and the corresponding EDS elemental mapping for the un-doped sample. The elemental mapping further demonstrates that the Sr element successfully entered into the bulk of the material. From the HRTEM image in Fig. 3b, the lattice fringes of (111), (131) and (020) corresponding to the monoclinic structure. Fig. 3h is the Fast Fourier transform (FFT) pattern taken from Fig. 3b. The FFT image is geometrically equivalent to a diffraction pattern and the appeared

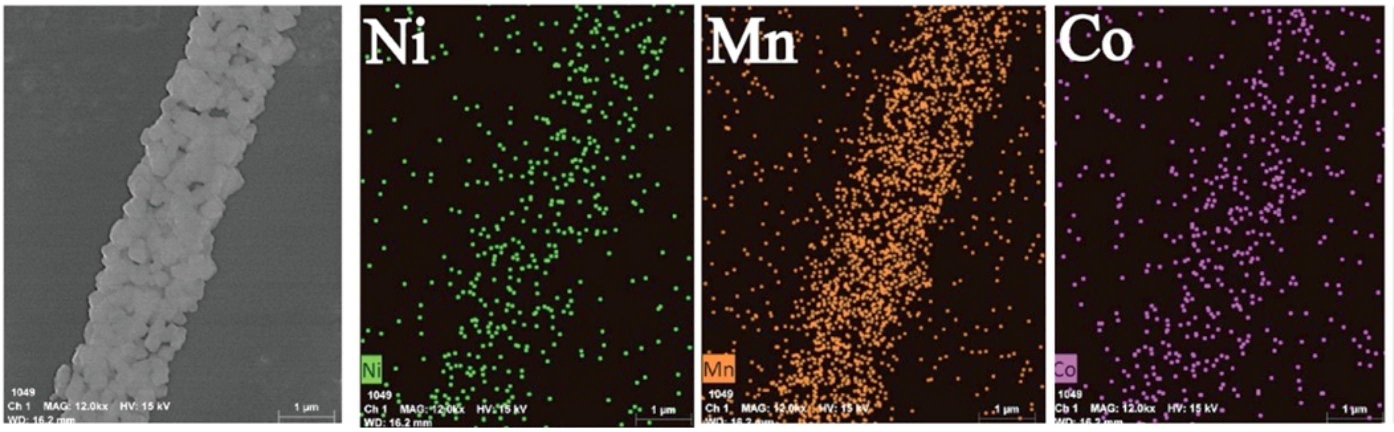

Fig. 4 The SEM image and the corresponding EDS elemental mapping of $Li_{1.2}Mn_{0.54}Ni_{0.13}Co_{0.13}O_2$.

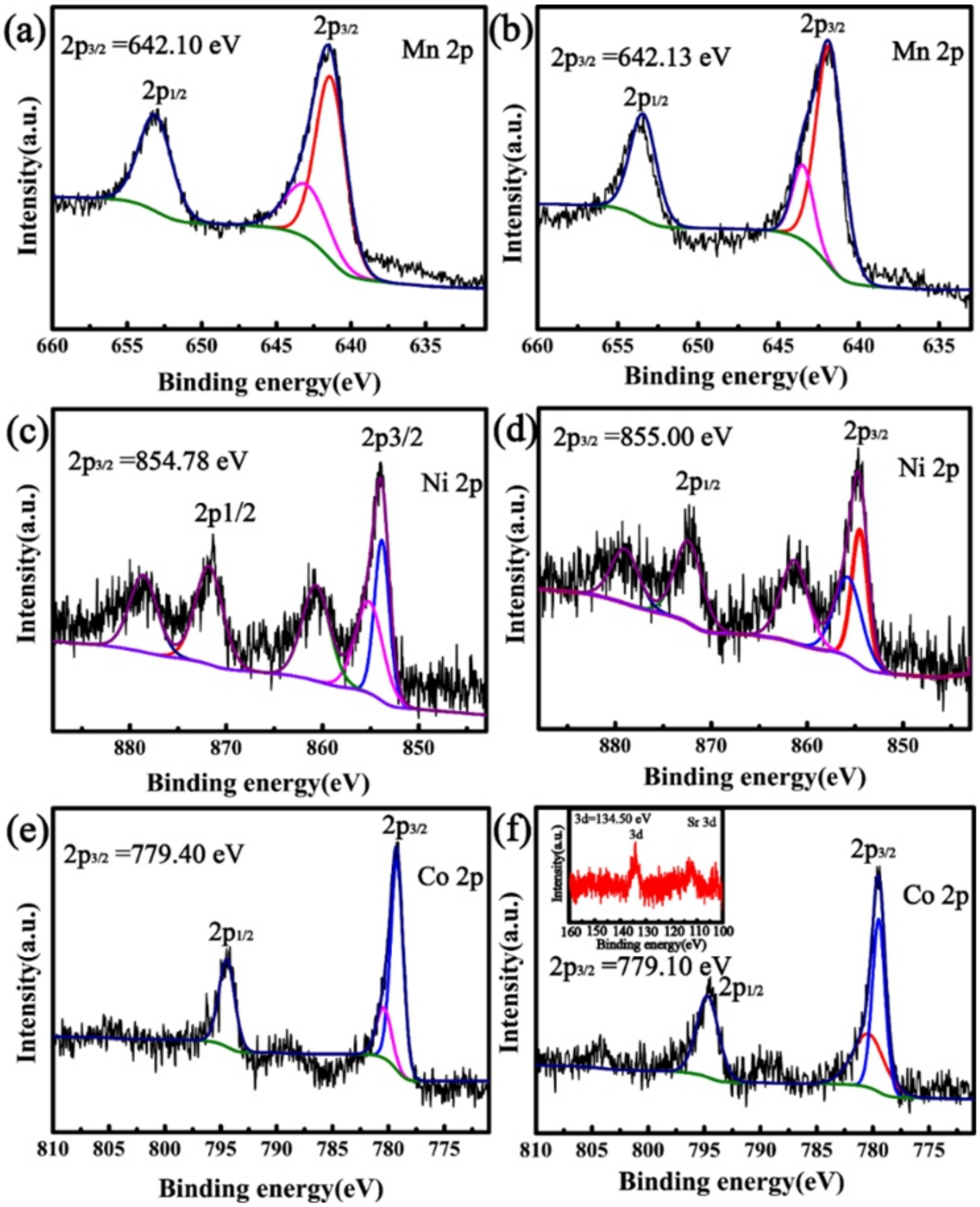

Fig. 5 XPS spectra of (a) Mn 2p, (c) Ni 2p and (e) Co 2p for sample $Li_{1.2}Mn_{0.54}Ni_{0.13}Co_{0.13}O_2$. XPS spectra of (b) Mn 2p, (d) Ni 2p and (f) Co 2p and Sr 3d for sample $Li_{1.2}Mn_{0.54}Ni_{0.13}Co_{0.10}Sr_{0.03}O_2$.

reflections can be indexed to the monoclinic structure (C2/m) of Li_2MnO_3.

XPS analysis

The oxidation states of the transition metals (Mn, Ni, Co and Sr) in the x=0 and x=0.03 samples were examined by X-ray photoelectron spectroscopy (XPS). The corresponding spectra of Mn 2p, Co 2p, Ni 2p and Sr 3d are presented in Fig. 5. As shown in Fig. 5(a-f), the peak positions of Mn $2p_{2/3}$, Ni $2p_{2/3}$ and Co $2p_{2/3}$ for two samples are very close to the data reported in references, indicating the presence of Mn^{4+}, Ni^{2+} and Co^{3+} in two samples.[32-33] The notable difference can be seen from the inset in Fig. 5(f) that in the binding energy region from 125 to 140 eV, sample $Li_{1.2}Mn_{0.54}Ni_{0.13}Co_{0.10}Sr_{0.03}O_2$ exhibits one strong speaks at about 134.5 eV, which could be well assigned to Sr 3d. It is well demonstrated[34] that the Sr element is present in sample $Li_{1.2}Mn_{0.54}Ni_{0.13}Co_{0.10}Sr_{0.03}O_2$ in the form of Sr^{2+}.

Electrochemical performance

The electrochemical performance of these cathode materials were investigate by assemble cells and the galvanostatic charge-discharge cycling was conducted at 28 mA g^{-1} in the voltage range of 2.0-4.8 V. Fig. 6(a-d) display the selected charge-discharge voltage profiles from the 1st to 100th cycles for sample $Li_{1.2}Mn_{0.54}Ni_{0.13}Co_{0.13-x}Sr_xO_2$ with doping ratio x = 0, 0.01, 0.03, 0.05, respectively. Clearly, during the first charging processes of these cathode materials, all profiles display a gradual increase in the voltage before 4.5 V along with a plateau at about 4.5 V. The smooth voltage ramp before 4.5 V could be correspond to the process of Ni^{2+} and Co^{3+} being oxidized to Ni^{4+} and Co^{4+}, and Li^+ being extracted from $LiMO_2$ component. Their high capacity was explained as being due to cumulative cationic ($M^{n+}\leftrightarrow M^{(n+1)+}$) and anionic

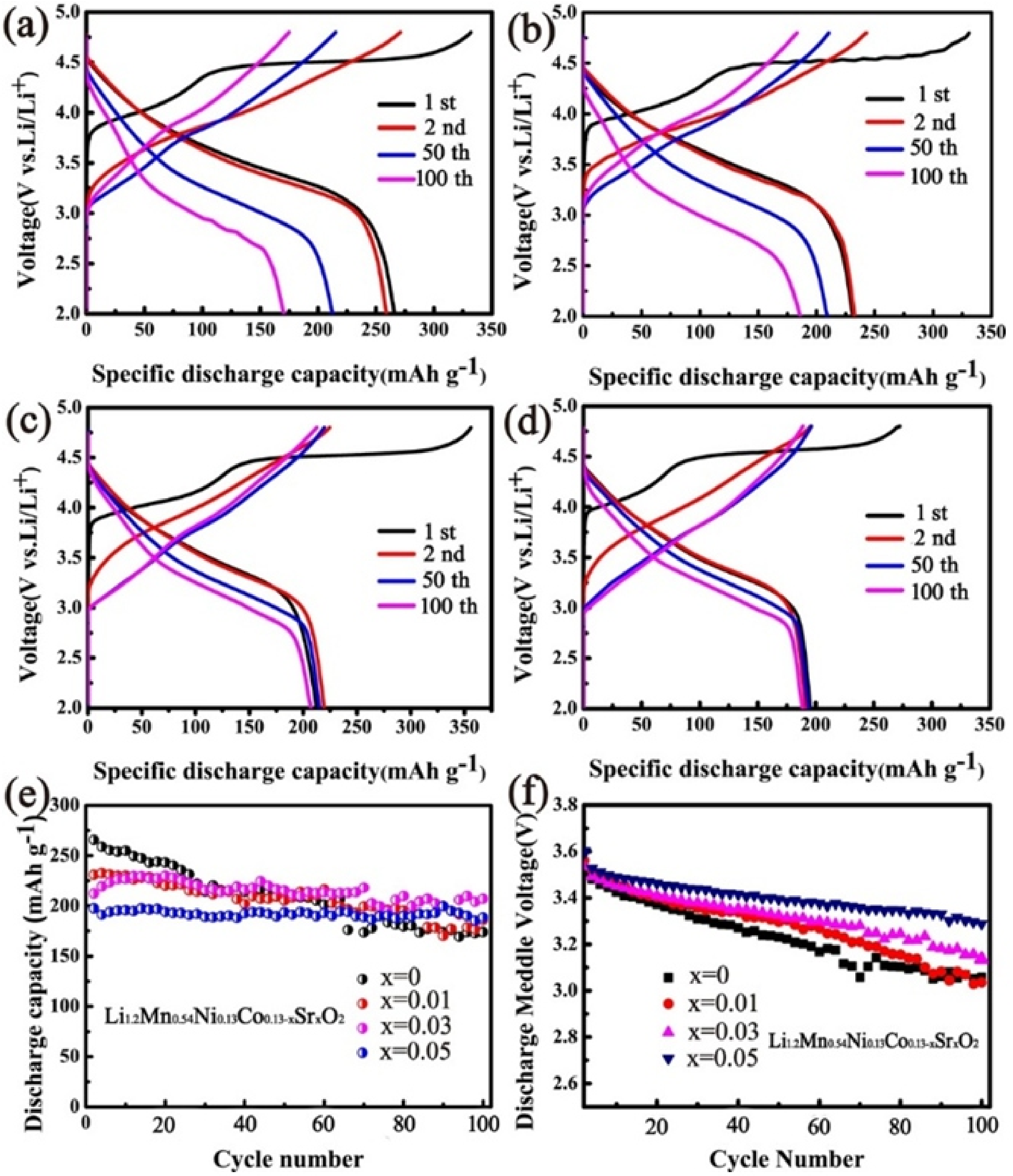

Fig. 6 Voltage profiles of $Li_{1.2}Mn_{0.54}Ni_{0.13}Co_{0.13-x}Sr_xO_2$ samples (a) x=0, (b) x=0.01, (c) x=0.03 and (d) x=0.05 electrodes at 28 mA g^{-1} in the potential range of 2.0-4.8 V. (e) Cycling performance of $Li_{1.2}Mn_{0.54}Ni_{0.13}Co_{0.13-x}Sr_xO_2$ (x=0, 0.01, 0.03, 0.05) electrodes. (f) The corresponding discharge meddle voltage vs. cycle number plots of $Li_{1.2}Mn_{0.54}Ni_{0.13}Co_{0.13-x}Sr_xO_2$ (x=0, 0.01, 0.03, 0.05) electrodes.

$(2O^{2-}\leftrightarrow(O_2)^{n-})$ reversible redox processes.[36] Tarascon and coworkers have suggested that oxidation of oxygen generally results in the pairing of O ions, resulting in an effective $2O^{2-}/O_2^{n-}$ redox couple, which is stabilized against evolution as oxygen gas in the presence of 4d and 5d TMs due to the increased TM–O hybridization and improved band alignment over 3d TMs.[36] William E. Gent *et al*. proposed that the properties arise from a strong coupling between anion redox and cation migration, which show that partially reversible transition metal migration decreases the potential of the bulk oxygen redox couple by > 1 V, leading to a reordering in the anionic and cationic redox potentials during cycling. [37]

Moreover, the first charging specific capacity of all the electrodes were found to be higher than 330 mAh g^{-1}, except for the $Li_{1.2}Mn_{0.54}Ni_{0.13}Co_{0.08}Sr_{0.05}O_2$ electrodes. These results indicate that appropriate amount of Sr doping does not influence the charging specific capacity and the initial activation process of the monoclinic Li_2MnO_3 phase in the first cycle. However, the first discharge specific capacities are found to be about 266, 231, 213 and 195 mAh g^{-1}, and the corresponding coulombic efficiencies are 80.6 %, 70 %, 62.6 % and 69.6 % for $Li_{1.2}Mn_{0.54}Ni_{0.13}Co_{0.13}O_2$, $Li_{1.2}Mn_{0.54}Ni_{0.13}Co_{0.12}Sr_{0.01}O_2$, $Li_{1.2}Mn_{0.54}Ni_{0.13}Co_{0.10}Sr_{0.03}O_2$ and $Li_{1.2}Mn_{0.54}Ni_{0.13}Co_{0.08}Sr_{0.05}O_2$ electrodes, respectively. The relatively low initial coulombic efficiency for the Sr doped cathode materials is ascribed to that the discharge capacity decreases with an increase in the Sr amount in these Li-rich cathodes whereas the charging capacity only slightly changes. According to previous studies, the decrease in the discharge capacity is possible related to that the substitution of a certain percentage of Co by Sr, which reduces the amount of Co redox species in the active mass.[38-40] As can be seen from the comparison of the selected voltage curves of all electrodes, the discharge specific capacity of the sample is becomes more and more concentrated as the amount of the Sr increases, indicating that the effect of Sr doping on stabilization materials is valid.

Fig. 6e presents the cycle performance of all electrodes at 28 mA g^{-1} rates in the potential range 2.0-4.8 V. As can be seen from Fig. 6e, the un-doped materials delivered an initial discharge capacity of 266 mAh g^{-1} and decreased to 174 mAh g^{-1} after 100 cycles, which gives the capacity retention is 64.5 %. On the contrast, the Sr-doped electrodes ($Li_{1.2}Mn_{0.54}Ni_{0.13}Co_{0.13-x}Sr_xO_2$ (x=0.01, 0.03, 0.05)) exhibit better cycling performance, and their capacity retention at the end of 100th cycles are 80.53 %, 94.16 % and 96.8 %, respectively. One attributes the voltage fade to the change of transition metal redox activities upon extended electrochemical cycling, and the other considers that structural rearrangement leads to the significant drop of the discharge voltage.[37] Anionic redox also leads to capacity loss and structural degradation, as well as voltage hysteresis, which shows the importance of controlling anionic redox reactions.[37] In order to investigate the effect of Sr doping on voltage decay, Fig. 6f compares the discharge meddle voltage profiles of four electrodes. It can be seen that the undoped electrode exhibits a rapid voltage degradation with the discharge meddle voltage decreasing from 3.46 V (1st cycle) to 2.73 V (100th cycle, ΔE=0.73 V) after 100 cycles at 28 mA g^{-1}. For $Li_{1.2}Mn_{0.54}Ni_{0.13}Co_{0.13-x}Sr_xO_2$ (x=0.01, 0.03, 0.05) electrodes, the discharge meddle voltage change upon cycling are 0.52 V, 0.39 V and 0.31 V, respectively. With the increase of the Sr doping ratio, the voltage change gradually decreases. Hence, the discharge voltage decay is effectively suppressed by Sr doping.

The first CV profiles of $Li_{1.2}Mn_{0.54}Ni_{0.13}Co_{0.13-x}Sr_xO_2$ (x=0, 0.01, 0.03, 0.05) are tested in the voltage range of 2.0–4.8 V vs. Li+/Li at a sweeping rate of 0.1 mV/s. as shown in Fig. 7. As can be seen from Fig. 7a, during the charge of the first cycle, there are two oxidation peaks at around 4.0 and 4.6 V. The 4.0 V peak is corresponds to the oxidation of Ni^{2+} to Ni^{4+} and Co^{3+} to Co^{4+}, which due to the extraction of Li^+ from $LiMO_2$. While the second sharp peak around 4.6 V originates from irreversible electrochemical activation of Li_2MnO_3 component. During the following discharge process, the reduction peaks around 4.25 and 3.7 V correspond to the reduction of Ni^{4+} and Co^{4+}, respectively. Besides, we can be observe that all samples display a pair of reversible redox peaks at 3.25 V, in consistent with the oxidation and reduction reaction of Mn^{3+}/Mn^{4+}. Fig. 7b shows the impedance spectra of $Li_{1.2}Mn_{0.54}Ni_{0.13}Co_{0.13-x}Sr_xO_2$ (x=0, 0.01, 0.03, 0.05) before cycle at open circuit potential. The inset in Fig. 7b exhibits the corresponding equivalent circuit model for fitting, where Rs, Rct, CPE, and Zw represent the resistance of electrolyte, the charge transfers resistance, the double layer capacitance, and the Warburg resistance, respectively. The Rct value of $Li_{1.2}Mn_{0.54}Ni_{0.13}Co_{0.13-x}Sr_xO_2$ (x= 0, 0.01, 0.03, 0.05) are 132.66 Ω, 116.88 Ω, 113.04 Ω, 112.43 Ω respectively, indicating that Sr-doping improves the conductivity of the sample.

To further reveal the electrochemical reactions that occurred during

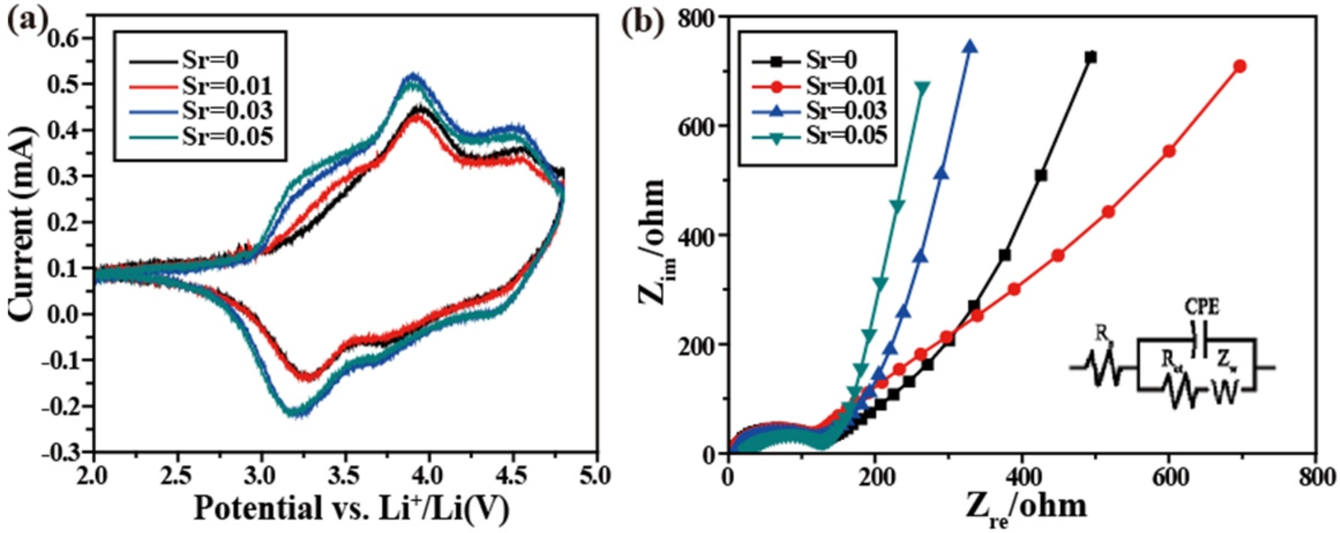

Fig. 7 (a) CV profiles of the first cycles of $Li_{1.2}Mn_{0.54}Ni_{0.13}Co_{0.13-x}Sr_xO_2$ (x= 0, 0.01, 0.03, 0.05). (b) EIS spectra of $Li_{1.2}Mn_{0.54}Ni_{0.13}Co_{0.13-x}Sr_xO_2$ (x= 0 , 0.01, 0.03, 0.05) electrodes.

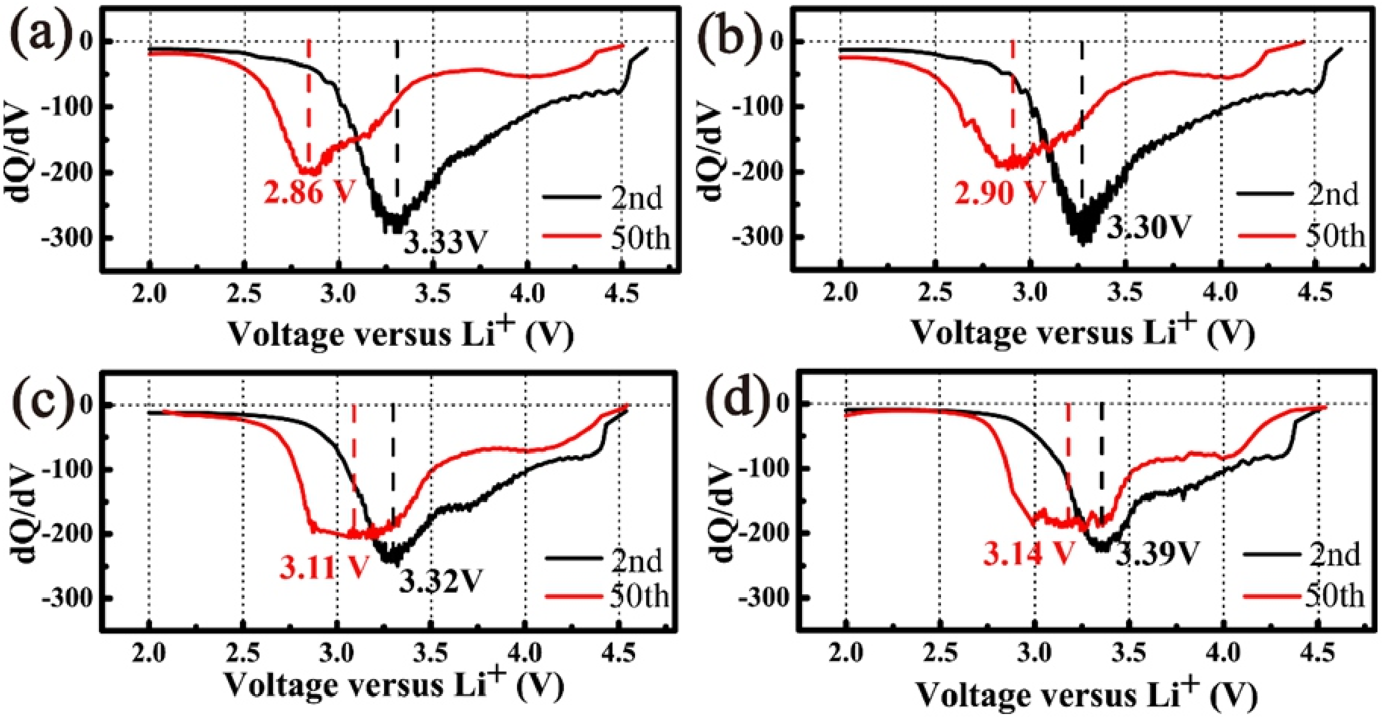

Fig. 8 The differential capacity dQ/dV vs. voltage plots for the 2nd and 50th cycles of $Li_{1.2}Mn_{0.54}Ni_{0.13}Co_{0.13-x}Sr_xO_2$ samples (a) x=0, (b) x=0.01, (c) x=0.03 and (d) x=0.05 electrodes measured at 0.1 C rate in the potential range of 2.0-4.8 V.

cycling, the differential capacity vs. voltage (dQ/dV) plots related to the 2nd and 50th cycles of all the electrodes are calculated from the numerical data observed in discharge profiles, as illustrated in Fig. 8. It is notable that the dQ/dV peaks corresponding to discharge profiles exhibit a distinct change upon the addition of Sr. There are three electrochemical processes centered at~4.5 V, ~3.7 V and lower than 3.5 V. Among them, the most dominant cathodic peaks appearing between 2.5 V and 3.2 V belong to the Mn^{4+}/Mn^{3+} redox activity, which are related to the layered-to-spinel phase transformation and deterioration of the generated spinel-like phase[42]. Therefore, comparing the cathodic peak potentials between the 2nd and 50th cycles is very necessary. As can be seen from Fig. 8, for un-doped electrodes, the cathodic peaks of Mn^{4+}/Mn^{3+} around 3.3 V transfer to a much lower voltage below 3.0 V after 50 cycles, which indicates the presence of spinel phase in the host structure. However, for the $Li_{1.2}Mn_{0.54}Ni_{0.13}Co_{0.10}Sr_{0.03}O_2$ electrode, the decrease of cathodic peak potential after 50 cycles is 0.21 V, which is much lower than those for the un-doped or slightly doped electrodes. These findings show that incorporation of suitable amount of Sr not only improves the capacity retention but also stabilizes the discharge voltage upon cycling.

Conclusions

To summarize, a facile way of synthesizing Sr doping hierarchical porous nanofiber structure lithium-rich material $Li_{1.2}Mn_{0.54}Ni_{0.13}Co_{0.13-x}Sr_xO_2$ was proposed. The Sr can be induced into Co site via electrospinning combined with high temperature solid phase technology. The Sr substitution for Co can enhance the cyclic performance, suppress the voltage decay and stabilize the structure. It is worth noting that the $Li_{1.2}Mn_{0.54}Ni_{0.13}Co_{0.10}Sr_{0.03}O_2$ material displays an initial discharge capacity of 213 mAh g^{-1} and the capacity retention is up to 94.16% after 100 cycles. Moreover, with the increase of Sr doping ratio, the voltage change after 100th cycle gradually decreases (ΔE=0.73 V for un-doped material and ΔE=0.31 V for $Li_{1.2}Mn_{0.54}Ni_{0.13}Co_{0.08}Sr_{0.05}O_2$). Thus, the structural stability of the material is effectively improved and the voltage decay is mitigated. Therefore, based on this work, these Sr-doping lithium-rich nanofibers with hierarchical pore structure materials will provide an effective and promising strategy for the synthesis of high energy density cathode materials for lithium ion batteries.

Acknowledgments

This work was supported by the National Science Foundations of China (grant no. 21471020, 21871028, and 21771024) and Beijing Municipal Natural Science Foundation (grant no. 2182029).

Compliance with ethical standards

Conflict of interest: The authors declare no conflict of interest.

References

1. Armand JMTM, *Nature*, 2001, **414**, 359-367.
2. Y Zhang, T. J. Zhu, L. Lin, M. W. Yuan, H. F. Li, G. B. Sun and S. L. Ma, *J. Nanopart. Res.*, 2017, **19**, 373(1-11).
3. N. Yabuuchi, K. Yoshii, S. T. Myung, I. Nakai and S. Komaba, *J. Am. Chem. Soc.*,2011,**133**, 4404.
4. M. M. Thackeray, S. H. Kang, C. S. Johnson, J. T. Vaughe, R. Benedek and S. A. Hackney, *J. Mater. Chem.*, 2007, **17**, 3112.
5. H. F. Li, J. Pang, Y. P. Yin, W. D. Zhuang, H. Wang, C. X. Zhai and S. G. Lu, *RSC Adv.*, 2013, **3**, 13907–13914.
6. T. Zhao, L. Li, R. Chen, H. Wu, X. Zhang, S. Chen, M. Xie, F. Wu, J. Lu and K. Amine, *Nano Energy*, 2015, **15**, 164-176.
7. G. Kobayashi, Y. Irii, F. Matsumoto, A. Ito, Y. Ohsawa, S. Yamamoto, Y. Cui, J. Y. Son and Y. Sato, *J. Power Sources*, 2016, **303**, 250-256.
8. B. Qiu, J. Wang, Y. Xia, Z. Wei, S. Han and Z. Liu, *ACS Appl. Mater. Interfaces*,2014, **6**, 9185-93.
9. F. Wu, N. Li, Y. Su, L. Zhang, L. Bao, J. Wang, L. Chen, Y. Zheng, L. Dai, J. Peng and S. Chen, *Nano Lett.*, 2014, **14**, 3550-5.

10. T. Tang and H. L. Zhang, *Electrochim. Acta*, 2016, **191**, 263-269.
11. P. K. Nayak, J. Grinblat, M. Levi, E. Levi, S. Kim, J. W. Choi and D. Aurbach, *Adv. Energy Mater.*, 2016, **6**, 1502398.
12. Z. Huang, Z. Wang, H. Guo and X. Li, *J. Alloys Compd.*, 2016, **671**, 479-485.
13. X. Jin, Q. Xu, H. Liu, X. Yuan and Y. Xia, *Electrochim. Acta*, 2014, **136**, 19-26.
14. Q. Li, G. Li, C. Fu, D. Luo, J. Fan and L. Li, *ACS Appl. Mater. Interfaces*, 2014, **6**, 10330-41.
15. J. Ma, Y. N. Zhou, Y. Gao, Q. Kong, Z. Wang, X. Q. Yang and L. Chen, *Chemistry*, 2014, **20**, 8723-30.
16. Y. Zang, C. X. Ding, X. C. Wang, Z. Y. Wen and C. H. Chen, *Electrochim Acta*, 2015, **168**, 234-239.
17. X. Wei and Y. Ren, *Electrochim. Acta*, 2015, **180**, 323-329.
18. L. Sun, X. Yi, X. Ren, P. Zhang and J. Liu, *J. Electrochem. Soc.*, 2016, **163**, A766-A772.
19. S. Kang, H. Qin, Y. Fang, X. Li and Y. Wang, *Electrochim. Acta*, 2014, **144**, 22-30.
20. R. Yu, G. Wang, M. Liu, X. Zhang, X. Wang, H. Shu, X. Yang and W. Huang, *J. Power Sources*, 2016, **335**, 65-75.
21. S. Valanarasu and R. Chandramohan, *J. Alloys Compd.*, 2010, **494**, 434-438.
22. G. Ting-Kuo, V. S. Fey, and Jian-Ging Chen, *Mater. Let.*, 2002, **52**, 197–202.
23. A. Subramania, N. Angayarkanni and T. Vasudevan, *J. Power Sources*, 2006, **158**, 1410-1413.
24. Z. Lu and J. R. Dahn, *J. Electrochem. Soc.*, 2003, **150**, A1044.
25. J. Li, R. Klöpsch, M. C. Stan, S. Nowak, M. Kunze, M. Winte and S. Passerini, *J. Power Sources*, 2011, **196**, 4821-4825.
26. Christopher S. Johnson, N. Li, Christina Lefief, John T. Vaughey and Michael M. Thackeray, *Chem. Mater.*, 2008, **20**, 6095–6106.
27. G. Singh, R. Thomas, A. Kumar, R. S. Katiyar, A. Manivannan, *J. Electrochem. Soc.*, 2012, **159**, A470.
28. Y. P. Deng, F. Fu, Z. G. Wu, Z. W. Yin, T. Zhang, J. T. Li, L. Huang and S. G. Sun, *J. Mater. Chem. A*, 2016, **4**, 257-263.
29. C. Venkateswara Rao, A. Leela Mohana Reddy, Y. Ishikawa and P. M. Ajayan, *ACS Appl. Mater. Interfaces*, 2011, **3**, 2966-72.
30. F. Amalraj, D. Kovacheva, M. Talianker, L. Zeiri, J. Grinblat, N. Leifer, G. Goobes, B. Markovsky and D. Aurbach, *J. Electrochem. Soc.*, 2010, **157**, A1121.
31. A. Abouimrane, O. C. Compton, H. Deng, I. Belharouak, D. A. Dikin, S. T. Nguyen and K. Amine, *Electrochem. Solid ST*, 2011, **14**, A126.
32. D. Ma, P. Zhang, Y. Li and X. Ren, *Sci. Rep.*, 2015, **5**, 11257.
33. A. Grimaud, W. T. Hong, Y. Shao-Horn and J. M. Tarascon, *Nat. Mater.*, 2016, **15**, 121-126.
34. Z. X. Hao, R. Zeng, L. X. Yuan, Q. M. Bing, J. Y. Liu, J.W. Xiang, Y. H. Huang, Nano Energy, 2017, **40**, 360-368.
35. W. E. Gent, K. Lim, Y. F. Liang, Q. H. Li, T. Barnes, S. J. Ahn, K. H. Stone, M. McIntire, J. Y. Hong, J. H. Song, Y. Y. Li, A. Mehta, S. Ermon, T. Tyliszczak, .D. Kilcoyne, D. Vine, J. H. Park, S. K. Doo, M.F. Toney, W. L. Yang, D. Prendergast and W. C. Chueh, *Nat. Commun.*, 2017, **8**, 2091.
36. L. Biao and D. G. Xia, *Adv. Mater.*, 2017, **29.**
37. W. L. Yang, *Nature Energy*, 2018, **3**, 619-620.
38. Y. Feng, E. Witkoske, E. Bell, Y. Wang, A. Tzempelikos, I. Ferguson and N. Lu, ES Mater. Manuf., 2018, **1**, 13-20.
39. C. Sekine, H. Osanai, K. Ikemori, R. Nakajima, S. Deminami, J. Sirimart and H. Gotou, ES Mater. Manuf., 2018, **1**, 35-40.
40. X. Zhao, P. Yang, L. Yang, Y. Cheng, H. Chen, H. Liu, G. Wang, V. Murugadoss, S. Angaiah and Z. Guo, ES Mater. Manuf., 2018, **1**, 67-71.